3d Transition-Metal-Mediated Columbite Nanocatalysts for Decentralized Electrosynthesis of Hydrogen Peroxide

Chang Liu, Hao Li, Junsheng Chen, Zixun Yu, Qiang Ru, Shuzhou Li, Graeme Henkelman, Li Wei,* and Yuan Chen*

Decentralized electrosynthesis of hydrogen peroxide (H_2O_2) via oxygen reduction reaction (ORR) can enable applications in disinfection control, pulping and textile bleaching, wastewater treatment, and renewable energy storage. Transition metal oxides are usually not efficient catalysts because they are more selective to produce H_2O. Here, it is shown that divalent 3d transition metal cations (Mn, Fe, Co, Ni, and Cu) can control the catalytic activity and selectivity of columbite nanoparticles. They are synthesized using polyoxoniobate ($K_7HNb_6O_{19}\cdot 13H_2O$) and divalent metal cations by a hydrothermal method. The optimal $NiNb_2O_6$ holds an H_2O_2 selectivity of 96% with the corresponding H_2O_2 Faradaic efficiency of 92% in a wide potential window from 0.2 to 0.6 V in alkaline electrolyte, superior to other transition metal oxide catalysts. Ex situ X-ray photoelectron and operando Fourier-transformed infrared spectroscopic studies, together with density functional theory calculations, reveal that 3d transition metals shift the d-band center of catalytically active surface Nb atoms and change their interactions with ORR intermediates. In an application demonstration, $NiNb_2O_6$ delivers H_2O_2 productivity up to 1 mol_{H2O2} g_{cat}^{-1} h^{-1} in an H-shaped electrolyzer and can yield catholytes containing 300×10^{-3} M H_2O_2 to efficiently decomposing several organic dyes. The low-cost 3d transition-metal-mediated columbite catalysts show excellent application potentials.

1. Introduction

Hydrogen peroxide (H_2O_2) is an essential chemical with a global production capacity of over 5.5 MT in 2015.[1,2] H_2O_2 as an environmentally friendly oxidizing agent and a potential liquid fuel, has a wide range of applications in disinfection control,[3] chemical synthesis,[4] pulping and textile bleaching,[5] wastewater treatment,[6] and renewable energy storage.[7] Over 95% of H_2O_2 is currently produced by the energy and material intensive hydrogenation-oxidation cycle of anthraquinone, which also requires Pd-based precious metal catalysts and additional transportation and distribution of hazardous high concentration H_2O_2.[8] Alternatively, H_2O_2 may be synthesized by directly reacting H_2 with O_2 over precious metal catalysts at low temperatures.[9] However, the slow kinetics of the direct H_2 and O_2 reaction and explosive H_2/O_2 mixtures are substantial hurdles for practical applications. The cathodic 2e⁻ oxygen reduction reaction (ORR) as an H_2O_2 production method was first reported in 1939.[10] Based on this method, the Huron–Dow process achieved industrial-scale production as small on-site units for the pulp industry in early 1990.[11] The growing interest in developing decentralized H_2O_2 production methods has fuelled recent research interests in developing fuel-cell type H_2O_2 production units and other innovative designs.[12,13]

These H_2O_2 production units require electrocatalysts to overcome ORR's activation energy barrier while retaining high selectivity to synthesize H_2O_2 via the 2e⁻ ORR pathway rather

C. Liu, J. Chen, Z. Yu, Dr. G. L. Wei, Prof. Y. Chen
School of Chemical and Biomolecular Engineering
The University of Sydney
Darlington, NSW 2006, Australia
E-mail: l.wei@sydney.edu.au; yuan.chen@sydney.edy.au

Dr. H. Li,[+] Prof. G. Henkelman
Department of Chemistry and the Oden Institute for Computational and Engineering Sciences
The University of Texas at Austin
105 E. 24th Street, Stop A5300, Austin, TX 78712, USA

Prof. Q. Ru
Guangdong Engineering Technology Research Center of Efficient Green Energy and Environmental Protection Materials
Guangdong Provincial Key Laboratory of Quantum Engineering and Quantum Materials
School of Physics and Telecommunication Engineering
South China Normal University
Guangzhou 510006, P. R. China

Prof. S. Li
School of Materials Science and Engineering
Nanyang Technological University
50 Nanyang Avenue, Singapore 639798, Singapore

than the $4e^-$ pathway to produce H_2O. For this purpose, commonly used electrocatalysts are based on precious metals, such as Pt, Pd, Au, and their alloys with Hg.[14] The scarcity and high cost of precious metals limit their broad applications, while the use of toxic Hg also raises environmental concerns. Alternatively, carbon-based catalysts, including oxidized carbon nanotubes, partially reduced graphene oxides, and doped carbon materials, have shown good performance.[15] However, carbon catalysts may suffer from stability issues in harsh alkaline electrolytes.[1] Therefore, the development of cost-effective and more stable transition metal-based catalysts, such as Fe_3O_4, WO_3, CeO_2, Ta_2O_5, Nb_2O_5, and V_xO_y, has drawn research interests.[16,17] Various approaches have been used to optimize the performance of these catalysts.[18] However, transition metal oxides' usefulness has been considered low because they are often intrinsically efficient catalysts for the $4e^-$ ORR.[13] Current research has suggested that the catalytic activity of transition metal oxides for ORR depends on interactions between the d-electrons of transition metals and the p-electrons of oxygen intermediates.[19] Forming bimetallic oxides may change the d-electron distributions in transition metals. For example, bimetallic Ru-Mn oxides show nearly 100% selectivity toward H_2O_2, although Ru is still a precious metal.[20] Alternatively, niobium pentoxide (Nb_2O_5) also shows catalytic activity toward H_2O_2.[17,21] Niobium (Nb) is a low-cost metal with a price of around US$40 kg^{-1}, which is well suited as a catalyst for broad adoption to cut down production costs. We envision that it may be possible to tailor Nb's d-electron distributions using transition metals to create high-performance Nb-based catalysts for the electrosynthesis of H_2O_2.

Herein, we used polyoxoniobate ($K_7HNb_6O_{19}\cdot 13H_2O$) prepared by molten salt reaction and divalent metal cations to synthesize a series of columbites by a hydrothermal method.

They are Nb based bimetallic oxide nanoparticles with a chemical formula of MNb_2O_6, where M represents 3d transition metals, including Mn, Fe, Co, Ni, or Cu. The incorporation of 3d transition metals to columbites changes the d-electron distributions of Nb. Comprehensive physicochemical characterizations were carried out to examine the properties of MNb_2O_6. Electrocatalytic performance tests reveal a volcano shape trend among the H_2O_2 selectivity of MNb_2O_6 containing different 3d transition metals, and $NiNb_2O_6$ shows the optimal catalytic performance. Ex situ X-ray photoelectron spectroscopy (XPS) and operando Fourier-transformed infrared spectroscopy (FTIR) were applied to determine the active catalytic sites in $NiNb_2O_6$. Density functional theory (DFT) calculations were further performed to understand 3d transition metals' role in mediating the d-electron distribution of Nb and possible correlations between the Nb d-band center and the catalytic performance of MNb_2O_6. Finally, the optimal catalyst was applied in an H-shaped electrolyzer. Electrosynthesis of H_2O_2 and its application for organic dye removals were demonstrated.

2. Results and Discussion

Figure 1a illustrates the synthesis of the series of 3d transition metal-mediated columbites (MNb_2O_6, M = Mn, Fe, Co, Ni, and Cu) using polyoxoniobate ($K_7HNb_6O_{19}\cdot 13H_2O$) and various divalent metal cations by a hydrothermal method. The freshly prepared $K_7HNb_6O_{19}\cdot 13H_2O$ exhibits three sharp peaks in its FTIR spectrum (Figure S1 in the Supporting Information), which are assigned to the vibrations of the terminal Nb-O_t (850 cm^{-1}) and bridging Nb-O_b-Nb (685 and 530 cm^{-1}) bonds, respectively.[22] After the hydrothermal reaction, solid powders of different colors were recovered and thermally annealed at
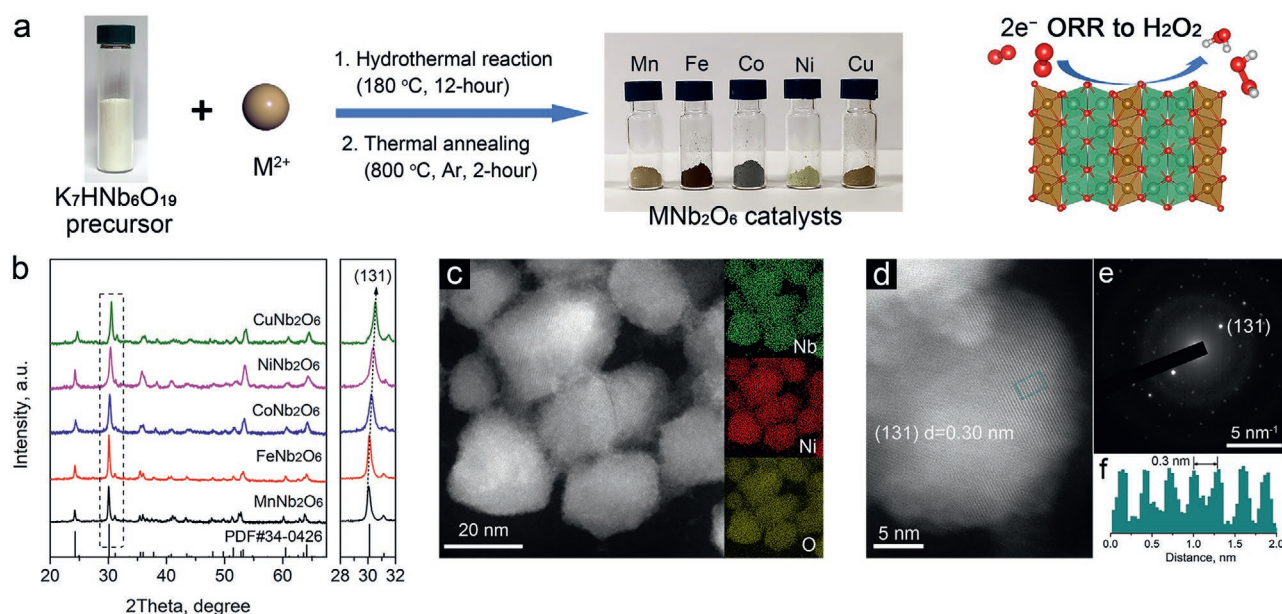

Figure 1. a) Schematic illustration of the synthesis of 3d transition metal-mediated columbites as catalysts for the direct electrosynthesis of H_2O_2. b) XRD patterns of columbites in comparison to a $FeNb_2O_6$ standard sample (PDF#34-0426). c) A HAADF-STEM image and the corresponding EDX mapping results of Nb, Ni, and O and d) a high-resolution TEM image of $NiNb_2O_6$. f) The line intensity profile of the selected area (green box) in (d) and e) its corresponding SAED pattern.

ADVANCED
SCIENCE NEWS
www.advancedsciencenews.com

NANO · MICRO
small
www.small-journal.com

Table 1. Physiochemical properties of different MNb_2O_6 and the reference Nb_2O_5.

	Grain size [nm]	Surface area [$m^2 g^{-1}$]	Metal ratio (M:Nb)[a]	Metal ratio (M:Nb)[b]
$MnNb_2O_6$	18.5	77.1	0.51	0.51
$FeNb_2O_6$	20.1	72.3	0.50	0.49
$CoNb_2O_6$	19.9	70.9	0.51	0.50
$NiNb_2O_6$	20.2	74.1	0.49	0.50
$CuNb_2O_6$	21.8	76.5	0.50	0.49
Nb_2O_5	23.0	65.8	–	–

[a] By XPS survey scan; [b] By ICP-AES measurement.

800 °C in Ar flow to obtain columbite nanoparticles. Nb_2O_5 and NiO nanoparticles were also synthesized as reference catalysts for comparison.

Various characterization techniques were used to determine the physicochemical properties of synthesized columbites. Figure 1b displays their powder X-ray diffraction (PXRD) patterns in comparison to a $FeNb_2O_6$ standard reference (PDF#34-0426, orthorhombic, space group: *Pcan*). All samples exhibit identical columbite characteristic peaks. The 2θ diffraction peaks at 24.3°, 30.1°, 35.5°, and 53.2° can be assigned to (111), (131), (002), and (621) facets, respectively. There are small peak shifts among various MNb_2O_6, as exemplified by the change in (131) diffraction peak in the right panel of Figure 1b, which can be attributed to the different ionic radius of the 3d transition metals.[23] Besides, no XRD peaks of 3d- transition metal oxides or Nb_2O_5 were observed. The crystallite grain size of MNb_2O_6 was calculated by the Scherrer equation, and the results are listed in **Table 1**. All MNb_2O_6 exhibit a similar grain size of about 19–22 nm. Their N_2 physisorption isotherms are also comparable (see Figure S2a in the Supporting Information), with a similar Brunauer–Emmett–Teller (BET) surface area of around 71–77 $m^2 g^{-1}$, as listed in Table 1. The Barrett–Joyner–Halenda (BJH) pore size distribution of all MNb_2O_6 samples are similar (Figure S2b in the Supporting Information), exhibiting major mesopores at ≈15 nm.

Scanning transmission electron microscope (STEM) images of MNb_2O_6 were taken under the high-angle annular dark-field mode (HAADF-STEM). As shown in Figure 1d and Figure S3 in the Supporting Information, all MNb_2O_6 display as cuboid nanoparticles with similar sizes of about 20–30 nm, consistent with that determined from their PXRD patterns. The corresponding energy-dispersive X-ray spectroscopic (EDX) elemental mapping results indicate that 3d transition metals, Nb, and O atoms are uniformly distributed in MNb_2O_6 nanoparticles. The elemental composition results also showed good agreement to that obtained by XPS survey scan and inductively coupled plasma atomic emission spectroscopy (ICP-AES) measurement. Figure 2e shows clear lattice fringes in the high-resolution TEM image of $NiNb_2O_6$. The histogram (Figure 2f) of the selected area (in the green box) exhibits a d-spacing of 2.95–3.00 Å, corresponding to the (131) facet of $NiNb_2O_6$. The selected area electron diffraction (SAED) pattern shown in Figure 2e confirms that $NiNb_2O_6$ nanoparticles are highly crystallized.

The atomic ratio between 3d transition metals and Nb in synthesized columbites is close to 1: 2, as confirmed by ICP-AES (Table 1). Their XPS survey scans show similar metal element ratios (Figure S4 in the Supporting Information). The high-resolution XPS spectra of M2p, Nb3d, and O1s in columbites are displayed in **Figure 2**a. All 3d transition metals exhibit two sets of peaks ($2p_{3/2}$ at the lower and $2p_{1/2}$ at the higher binding energies) as a result of the spin-orbital split. The Mn2p peaks at 640.4 eV ($2p_{3/2}$) and 652.3 eV ($2p_{1/2}$) resemble that of Mn^{2+}, which was further confirmed by the 6 eV energy gap in the Mn3s spectrum (Figure S5 in the Supporting Information).[24] The binding energy difference between the $2p_{3/2}$ and $2p_{1/2}$ peaks is 13.6 eV for Fe (710.2 and 723.8 eV), and 16.2 eV for Co (780.4 and 796.6 eV), respectively, suggesting that both cations are in the divalent state.[25] $Ni2p_{3/2}$ exhibits a single peak at 854.6 eV that resembles the peak of Ni^{2+}. Its line-shape also rules out the possible formation of phase-segregated NiO, which should display multiplet-split $2p_{3/2}$ peaks.[26] The signature dual-split $Cu2p_{3/2}$ satellite peaks confirm the existence of Cu^{2+}.[27] Nb3d and O1s XPS spectra collected from different columbites are identical. As shown in Figure 2b, $Nb3d_{5/2}$ and $3d_{5/2}$ peaks at 207.0 and 209.8 eV indicate the existence of Nb^{5+}. O1s spectra exhibit a sharp peak at ≈530 eV together with a weak and broad peak at ≈540 eV, which can be assigned to the lattice metal-oxygen (M−O) bonds and surface adsorbed water, respectively. Our comprehensive characterization results suggest that different columbites nanoparticles with the chemical formula of MNb_2O_6 have similar morphological and crystalline structures. This observation also suggests that the polyoxoniobate based hydrothermal synthesis approach can be further extended to prepare 3d-TM based tungstate and tantalate columbite nanoparticles.

We also characterized the reference Nb_2O_5 sample. Its XRD pattern confirms the formation of dominating T-Nb_2O_5 (orthorhombic, space group *Pbam*, Figure S6 in the Supporting Information). It has a particle size determined by TEM images (Figure S7 in the Supporting Information) at 35 ± 13 nm, comparable to that of MNb_2O_6 nanoparticles. The corresponding well-resolved SAED pattern can be assigned to its various crystal facets, consistent with its PXRD pattern. Additionally, its high-resolution XPS spectra of Nb3d and O1s are similar to those of MNb_2O_6 (Figure S8 in the Supporting Information).

The ORR catalytic performance of MNb_2O_6 and Nb_2O_5 was evaluated on rotary ring-disk electrode (RRDE) deposited with catalysts (200 μg cm^{-2}) in 0.1 M KOH electrolyte. **Figure 3**a displays the ring current (i_{ring}), and the disk current density (j_{disk}, over the surface area of the disk) of RRDEs loaded with different catalysts. It should be noted that the RRDE without depositing catalysts (bare glassy carbon) shows inferior catalytic performance toward H_2O_2 production with lower onset potentials and smaller currents (Figure S9 in the Supporting Information). The onset potentials for the disk and ring currents (U_{disk} and U_{ring}) were extracted and compared in **Table 2**.

$NiNb_2O_6$ exhibits the highest U_{disk} (0.72 V vs reversible hydrogen electrode (RHE)) and U_{ring} (0.69 V vs RHE) among all catalysts, indicating its superior catalytic activity for ORR. Under 0.2 V versus RHE, the MNb_2O_6 catalysts deliver comparable j_{disk} with the maximum difference of about 18% between $CoNb_2O_6$ (−1.50 mA cm^{-2}) and $CuNb_2O_6$ (−1.82 mA cm^{-2}).
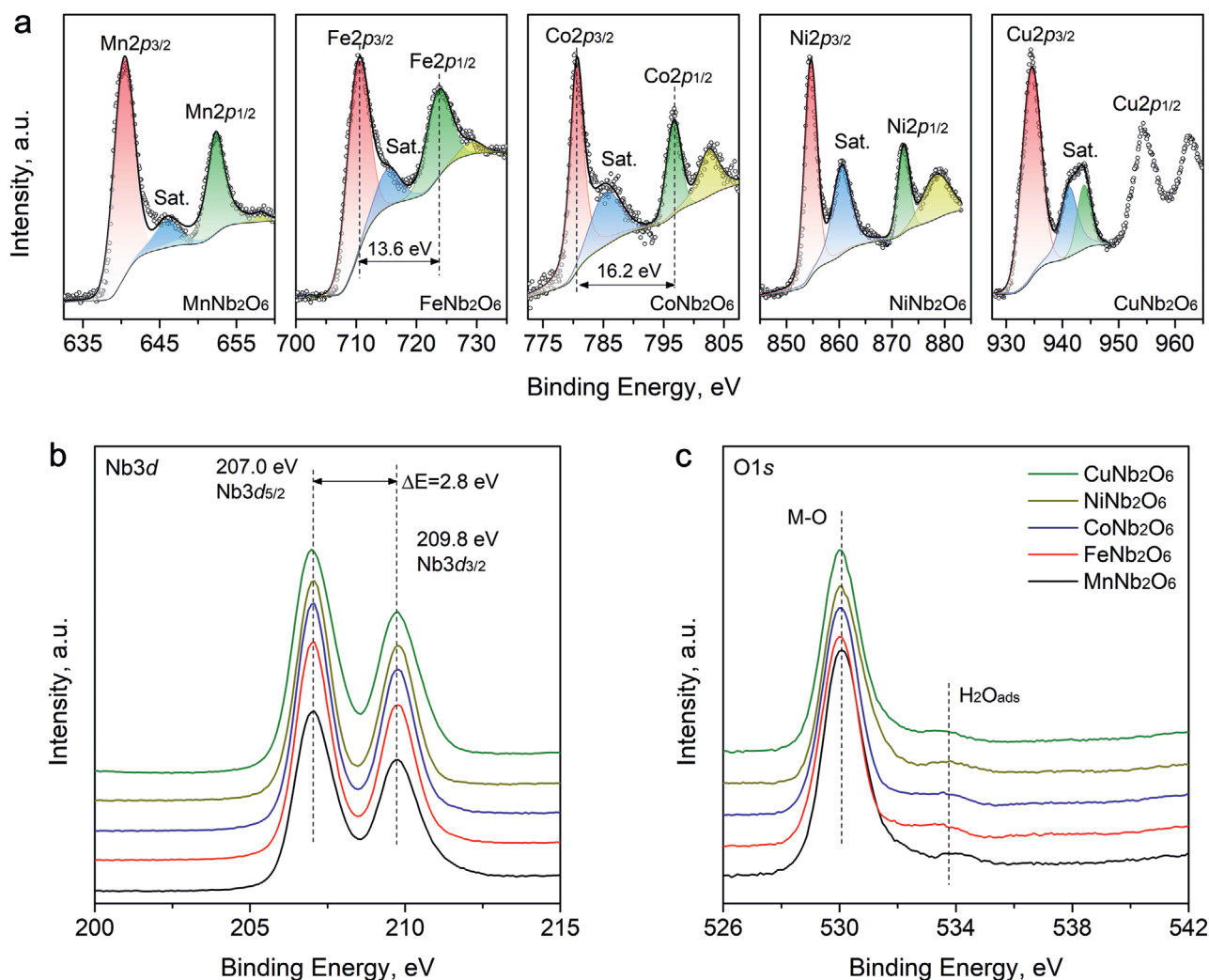
Figure 2. High-resolution XPS spectra of a) M2p features of the 3d-metals, b) Nb3d, and c) O1s in different columbites.

However, i_{ring} associated with H_2O_2 synthesis display substantial differences. $NiNb_2O_6$ has an i_{ring} of 0.14 mA, which is two times higher than that of $CoNb_2O_6$, $CuNb_2O_6$, and Nb_2O_5 and four times higher than that of $MnNb_2O_6$, indicating that $NiNb_2O_6$ has the highest selectivity toward H_2O_2 synthesis. We also normalized j_{disk} and i_{ring} based on the BET surface areas of the catalysts loaded on the disk of the RRDEs. $NiNb_2O_6$ also delivers the best activity among the MNb_2O_6 (Figure S10 in the Supporting Information). The selectivity toward H_2O_2 for MNb_2O_6 was calculated and displayed in Figure 3b. $NiNb_2O_6$ retains a selectivity of 96% with a corresponding H_2O_2 Faradaic efficiency of 92% in the wide potential window from 0.2 to 0.6 V versus RHE. Table 2 shows that H_2O_2 selectivity and the Faradaic efficiency of $NiNb_2O_6$ are higher than those of all other MNb_2O_6 catalysts. The electron transfer number (n) of $NiNb_2O_6$ is determined to be 2.09, indicating that ORR takes place on $NiNb_2O_6$ by the $2e^-$ pathway.

As shown in Figure 3d, the kinetic performance of MNb_2O_6 were assessed from Tafel plots. The kinetic current densities (j_K) were extracted using the K–L equation. The Tafel plots exhibit three regions with different slopes, suggesting changes in the

rate-determining step (RDS) when the applied overpotential increases (Table S1 in the Supporting Information).[28] At lower overpotentials (Region I, $\eta < 50$ mV), MNb_2O_6 and Nb_2O_5 have a slope between 80–90 mV dec^{-1}, suggesting that the RDS is the electron transfer in the formation of surface adsorbed $*O_2^-$ intermediates ($O_2 + * + e^- \rightarrow *O_2^-$).[29] At higher overpotentials (Region II, $50 < \eta < 125$ mV), the RDS becomes the formation of $*OOH$ intermediates via a proton transfer step ($*O_2^- + H^+ \rightarrow *OOH$) with the Tafel slope of ≈100–120 mV dec^{-1}. In the region III ($\eta > 125$ mV), the larger Tafel slopes (>200 mV dec^{-1}) indicate that the adsorption of O_2 is the RDS. Figure 3e shows that MNb_2O_6 and Nb_2O_5 have similar RDSs in these three regions. In particular, $NiNb_2O_6$ has the smallest Tafel slope among MNb_2O_6, indicating its superior reaction kinetics.

Importantly, we observed a volcano shape trend among the H_2O_2 selectivity of the different MNb_2O_6 catalysts, suggesting that the observed catalytic performance of MNb_2O_6 is correlated with the mediating effects different 3d transition metals. Compared to Nb_2O_5, Ni and Co-based MNb_2O_6 show higher H_2O_2 selectivity. In contrast, Mn, Fe, and Cu-based MNb_2O_6 catalyze ORR via the $4e^-$ pathway with lower H_2O_2 selectivity. We also

ADVANCED
SCIENCE NEWS
www.advancedsciencenews.com

NANO · MICRO
small
www.small-journal.com
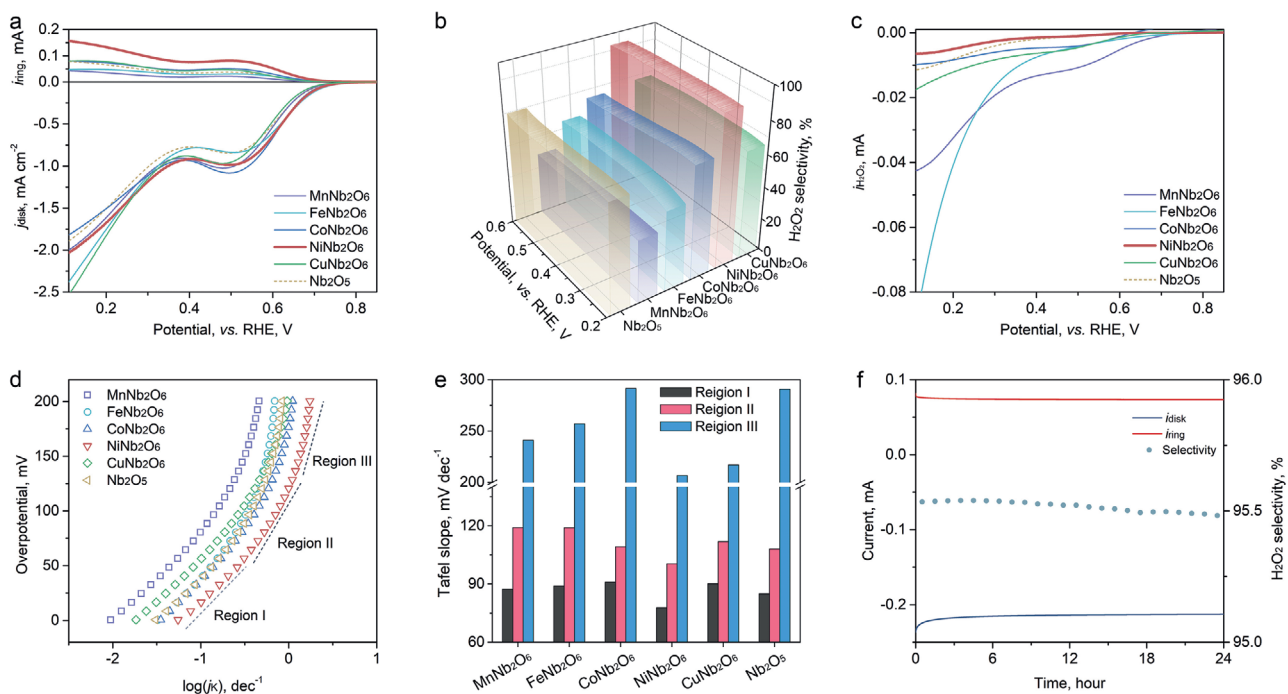
Figure 3. Catalytic performance of MNb_2O_6 for ORR. a) RRDE LSV curves collected in O_2-saturated 0.1 M KOH (pH = 12.6) and b) the H_2O_2 selectivity over the potential window from 0.2 to 0.6 V versus RHE. c) Background-corrected H_2O_2 reduction currents of MNb_2O_6 in an Ar-saturated 0.1 M KOH electrolyte containing 1×10^{-3} M H_2O_2. d) Tafel plots and e) the calculated Tafel slopes of MNb_2O_6 and Nb_2O_5. f) The stability of the catalytic performance of $NiNb_2O_6$ under 0.3 V versus RHE in O_2-saturated 0.1 M KOH.

measured the catalytic activity of MNb_2O_6 for H_2O_2 reduction reaction (H_2O_2RR) in Ar saturated 0.1 M KOH electrolyte containing 1×10^{-3} M H_2O_2. Figure 3c displays their linear sweep voltammetry (LSV) curves obtained at a scan rate of 2 mV s^{-1}. $NiNb_2O_6$ exhibits the lowest current and onset potential, indicating that $NiNb_2O_6$ is inert to H_2O_2 adsorption, which prevents the further reduction of H_2O_2 to H_2O, resulting in the high H_2O_2 selectivity.

We further assessed the stability of the catalytic activity of $NiNb_2O_6$. The chronoamperometric currents of the ring and disk electrodes were recorded in 50 mL of O_2 saturated 0.1 M KOH electrolyte, when they were biased at 0.3 and 1.4 V versus RHE, respectively. Figure 3f shows that both i_{disk} and i_{ring} remain stable through the 24 h test with negligible decay. The H_2O_2 selectivity was maintained at ≈95.5% during the entire test. LSV curves of $NiNib_2O_6$ at the beginning and after the stability test exhibit minimal differences (see Figure S11 in

the Supporting Information). We also characterized $NiNib_2O_6$ after the stability test by HAADF-STEM. Figure S12 in the Supporting Information shows that the morphology, crystallinity, and elemental distribution of $NiNib_2O_6$ remain unchanged after the stability test. Furthermore, $NiNib_2O_6$ also shows better performance compared with recently reported transition metal oxide-based catalysts (see Figure S13 and Table S2 in the Supporting Information).

Next, we carried out ex situ XPS analysis to identify the active catalytic site of $NiNb_2O_6$. **Figure 4**a shows that the O1s XPS spectrum exhibits substantial changes after the stability test. Two new peaks associated with hydroxides (531.7 eV) and oxygen in peroxides (532.4 eV) emerge.[30] Figure 4b shows that the XPS Ni2p spectrum has negligible changes in both peak positions and line-shapes compared with that of $NiNb_2O_6$ before ORR tests. In contrast, the binding energies of Nb $3d_{5/2}$ and Nb $3d_{3/2}$ shift ≈0.2 eV higher after the stability test (Figure 4c).

Table 2. Summary of the electrochemical performance of MNb_2O_6 and Nb_2O_5 for ORR.

	U_{disk} [V]	U_{ring} [V]	j_{disk}[a] [mA cm^{-2}]	i_{ring}[a] [mA]	H_2O_2 selectivity,[a] %	n	FE_{H2O2},[a] %
$MnNb_2O_6$	0.67	0.64	−1.61	0.035	39	3.22	24
$FeNb_2O_6$	0.68	0.65	−1.75	0.048	47	3.07	30
$CoNb_2O_6$	0.69	0.67	−1.50	0.077	73	2.55	57
$NiNb_2O_6$	0.72	0.69	−1.69	0.140	96	2.09	92
$CuNb_2O_6$	0.68	0.65	−1.82	0.077	64	2.72	47
Nb_2O_5	0.70	0.66	−1.50	0.066	66	2.69	49

[a]Catalytic activity collected under 0.2 V versus RHE.

ADVANCED
SCIENCE NEWS
www.advancedsciencenews.com

NANO · MICRO
small
www.small-journal.com
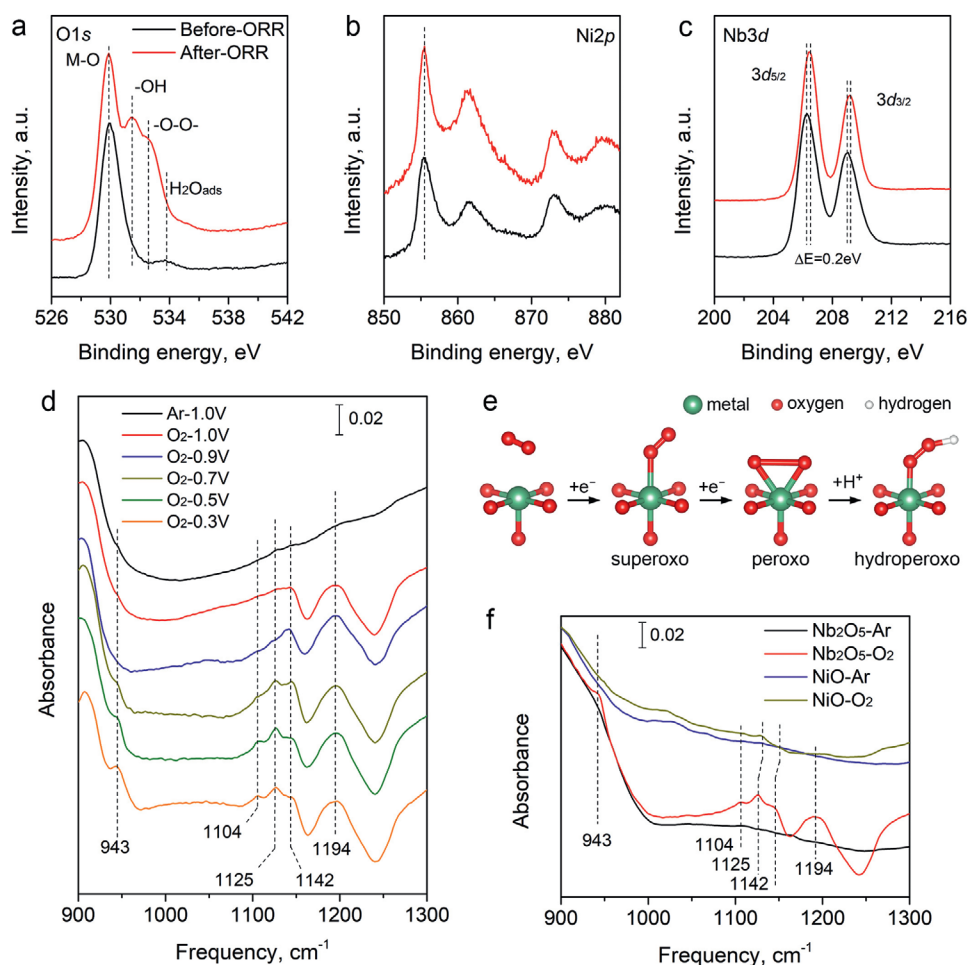
Figure 4. Ex situ and operando spectroscopic studies of the active catalytic site in $NiNb_2O_6$. Ex situ high-resolution XPS spectra of a) O1s, b) Ni2p, and c) Nb3d in $NiNb_2O_6$ before and after the 24 h ORR stability test. d) Operando FTIR spectra of $NiNb_2O_6$ during ORR biased at different potentials in Ar and O_2 saturated 0.1 M KOH. e) Schematic illustration of ORR intermediates adsorbed on the proposed surface metal site (their geometries are not optimized). f) Operando FTIR spectra of Nb_2O_5 and NiO biased at 0.5 V versus RHE in Ar and O_2 saturated 0.1 M KOH.

The increased binding energies of Nb3d indicate a decreased 3d electron density on Nb atoms, which may contribute to the electron transfer from Nb atoms to surface adsorbed oxygenous intermediates. These ex situ XPS results suggest that the active catalytic sites of $NiNb_2O_6$ for ORR are on Nb atoms.

We further used operando FTIR to identify the active catalytic site in $NiNb_2O_6$ in comparison with the studies of Nb_2O_5 and NiO reference catalysts. NiO nanoparticles have a comparable size of 24 ± 12 nm (see details in the Experimental Section and the TEM image in Figure S14 in the Supporting Information) but exhibit negligible ORR activity with an i_{ring} of merely 0.04 mA under 0.2 V versus RHE and an H_2O_2 selectivity of 50% (Figure S15 in the Supporting Information). Figure 4d shows the FTIR spectra of $NiNb_2O_6$ biased at 1.0 V versus RHE in Ar and O_2 saturated 0.1 M KOH electrolyte. The FTIR spectra of $NiNb_2O_6$ show substantial changes when the electrolyte is switched from Ar saturated KOH to O_2 saturated KOH. Two new peaks emerge at 1142 and 1194 cm^{-1}, which can be assigned to the stretching vibration of surface adsorbed superoxo (v_{O2}.) intermediates, as illustrated in Figure 4e.[31,32] Under cathodic potentials ≤0.7 V versus RHE, additional peaks appear

at 943 cm^{-1}, and 1104 and 1125 cm^{-1}, which can be attributed to surface bounded peroxo ($v_{O–O}$) and hydroperoxo intermediates, respectively, indicating the formation of surface-bonded OOH intermediates.

Based on the FTIR peak assignments on $NiNb_2O_6$, we further carried out operando FTIR analysis of Nb_2O_5 and NiO. Both were biased at 0.5 V versus RHE in Ar or O_2 saturated 0.1 M KOH electrolytes. Figure 4f shows that both Nb_2O_5 and NiO have the signature peaks assigned to various ORR intermediates. However, the peak intensity on NiO is much weaker than that on Nb_2O_5 and $NiNb_2O_6$. These results indicate that Ni sites are catalytically less active than Nb sites, consistent with the lower catalytic activity of NiO shown in Figure S15 in the Supporting Information. Besides, the peak positions on Nb_2O_5 are similar to those on $NiNb_2O_6$. In contrast, the peak positions on NiO shift to higher frequencies, which may be attributed to the fact that Ni (58.7 g mol^{-1}) has a smaller molecular weight than Nb (92.9 g mol^{-1}).[31] Collectively, ex situ XPS and operando FTIR results support the result that surface Nb atoms on $NiNb_2O_6$ are the active catalytic site for H_2O_2 synthesis.

**ADVANCED
SCIENCE NEWS**

www.advancedsciencenews.com

NANO · MICRO

small

www.small-journal.com
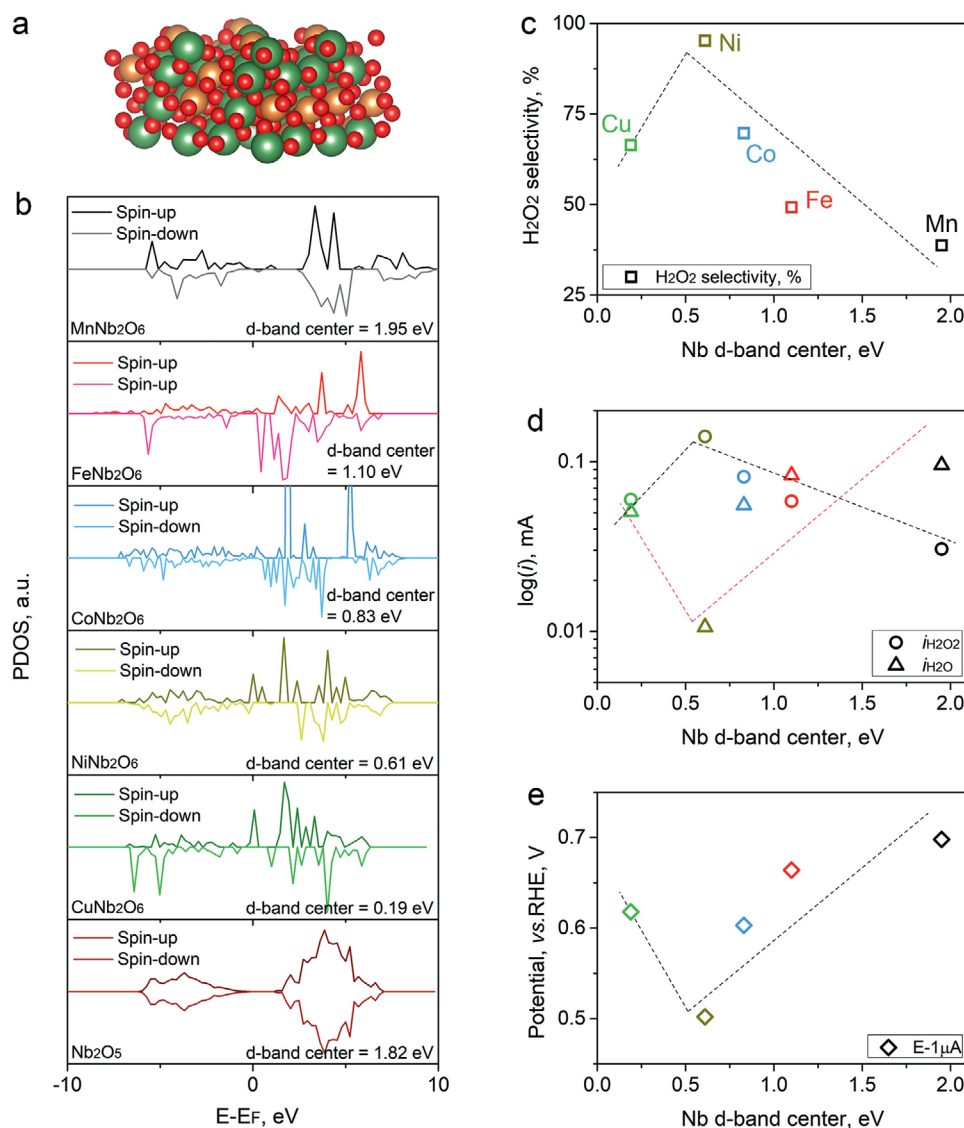
Figure 5. Calculations of the effect of 3d transition metals on the catalytic activity of MNb_2O_6. a) An atomic model of MNb_2O_6 slab exposing the {131} facet. Atom colors: orange-M, green-Nb, and red-O) and b) the calculated Nb PDOS in different MNb_2O_6. Correlations between the d-band center of Nb in MNb_2O_6 and ORR performance descriptors c) H_2O_2 selectivity, d) i_{H2O2} and i_{H2O}, and e) the onset potential of H_2O_2RR.

Next, we performed DFT calculations to investigate the mediating effect of different 3d transition metals on the catalytic activity of Nb active sites in MNb_2O_6. Based on our XRD and STEM measurement results (Figure 1), we calculated the projected density of states (PDOS) of Nb in different MNb_2O_6 slabs exposing the {131} facet, as schematically illustrated in **Figure 5**a. To assess the trends found from experiments, we used an analysis similar to the method by Stamenkovic et al.,[33] which correlates the experimental ORR performance with the d-band center of catalyst, as the d-band center is a proven key descriptor that describes the adsorption and catalytic capacities of metal oxides for ORR.[34] According to the Sabatier principle, an optimal catalytic surface should bind the adsorbate neither too strongly nor too weakly.[35] A d-band center of the system closer to the Fermi level generally leads to a stronger binding strength, while a value being far from the Fermi leads to the

weaker binding.[36] As shown in Figure 5b, the Nb d-band centers in various MNb_2O_6 columbites shift significantly compared to that of Nb_2O_5 (1.82 eV). The shifted Nb d-band centers affect the interaction between Nb and ORR intermediates, altering its catalytic activity in ORR toward H_2O_2 synthesis.[37] Consequently, various volcano-shaped trends can be established between Nb d-band centers of MNb_2O_6 and several ORR activity descriptors, including H_2O_2 selectivity (Figure 5c), and ORR ring currents (Figure 5d) and ring currents (Figure 5e). Besides, the onset potential of H_2O_2RR (defined as the potential required to reach the current of −0.1 μA, Figure 5f) also exhibits a reverse volcano shape, showing a good agreement with H_2O_2RR experimental results. These volcano-like correlations fulfill the Sabatier principle in catalysis,[35] and the volcano-shaped correlations found between ORR performance and d-band center are similar to the results by Stamenkovic

ADVANCED
SCIENCE NEWS
www.advancedsciencenews.com

NANO · MICRO
small
www.small-journal.com
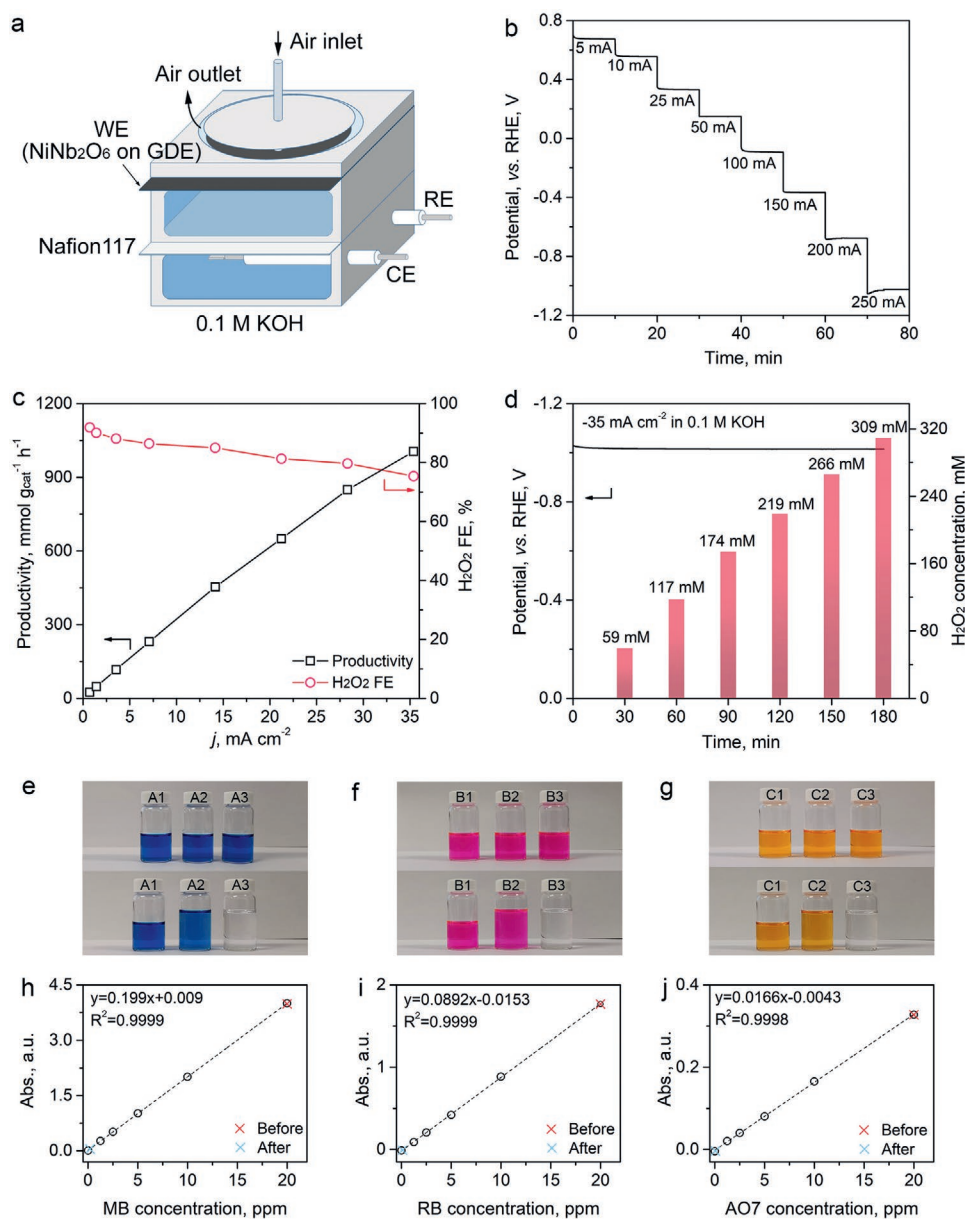
Figure 6. a) A schematic illustration of the prototype H_2O_2 electrolyzer for organic dye removal. b) Current-potential response and c) H_2O_2 production rate and H_2O_2 Faradic efficiency. d) Chronopotentiometric H_2O_2 production performance and the cumulative H_2O_2 concentration. e–g) Photos and h–i) the corresponding absorption calibration curves of dye solutions before (bottles labeled as 1) and after adding catholyte electrolyzed with N_2 (bottles labeled as 2) or O_2 (bottles labeled as 3) saturation. A refers to MB, B refers to RB, and C refers to AO7.

et al. on various Pt-group ORR catalytic systems.[33] We also calculated d-band centers of 3d transition metals in MNb_2O_6. The results are listed in Table S3 in the Supporting Information, and their PDOS profiles are displayed in Figure S16 in the Supporting Information. No correlations can be established between the d-band centers of the 3d transition metals with the ORR catalytic performance of MNb_2O_6, showing good agreement with our operando FTIR results that the 3d metal (for example, Ni) is not the active site. Based on these correlations, it is expected that the d-band center is an efficient reaction descriptor with minimal computation cost for the study of complicated transition metal oxide systems like MNb_2O_6

columbites. Due to the tremendous computational cost for these atomistic systems and the existence of many different sites on the metal oxide surfaces, we did not analyze the reaction free energy profile on these systems. We also expect that these empirical volcano-like correlations can help in the rapid screening of Nb-based metal oxides with high activity and selectivity.

Finally, the H_2O_2 productivity of the optimal $NiNb_2O_6$ columbite was evaluated in an H-shaped electrolyzer using 0.1 M KOH electrolyte, as illustrated in **Figure 6**a. The catalyst was loaded on a carbon gas diffusion layer as an electrode in the cathode chamber with an optimized mass loading of 0.5 mg cm^{-2}

**ADVANCED
SCIENCE NEWS**

www.advancedsciencenews.com

**NANO · MICRO
small**

www.small-journal.com

(Figure S17 in the Supporting Information) to overcome the O_2 dissolution limitation and diffusion barrier (see details in the Experimental Section).

The chronopotentiometric response of the electrolyzer collected at different currents is displayed in Figure 6b. Although the potential required to deliver a higher current gradually increases, the electrolyzer responds quickly to current changes, and the potential remains stable. We further assessed the H_2O_2 productivity by the colorimetric method (see details in the Experimental Section) under different operating current densities. As displayed in Figure 6c, the H_2O_2 productivity increases almost linearly with the increase of the current density, reaching a maximum of 996 $mmol_{H2O2}$ g_{cat}^{-1} h^{-1} under a current density of 35.4 mA cm^{-2}. The Faradaic efficiency of the electrolyzer decreases from 91.9% to 75.4% with the increase of the current density. We further tested the stability of the electrolyzer by discharging at 35.4 mA cm^{-2} for 3 h. Figure 6d shows that it works steadily and delivers a catholyte containing up to 309 × 10^{-3} M H_2O_2 after the 3 h test. H_2O_2 solutions at this concentration can be used for pulp/paper bleaching[5] or oxidative decontamination of wastewater.[6] We further demonstrated the use of the catholyte for organic dye removals via Fenton reactions. As shown in Figure 6e–g, we selected three organic dyes commonly used in the textile industry, including MB, RB, and AO7. After adding 5 mL of the acidified catholyte prepared by discharging the electrolyzer under the current density of 35.4 mA cm^{-2} for 30 min, the bright colors of dye solutions (20 ppm) quickly disappeared (bottle 3). In comparison, adding catholytes saturated with N_2 during discharging (bottle 2) show no color changes. Figure 6h–j show that the dye degradation efficiencies quantified by UV–vis absorption spectroscopy are close to unity for the three dyes (i.e., 99.5 ± 0.3% for MB, 99.7±0.4% for RB, and 99.8±0.2% for AO7, respectively).

3. Conclusion

Columbite (MNb_2O_6) crystalline nanoparticles were synthesized using $K_7HNb_6O_{19}·13H_2O$ and 3d transition metal salts (Mn, Fe, Co, Ni, and Cu). They demonstrate excellent catalytic performance as ORR catalysts for the electrosynthesis of H_2O_2. Different MNb_2O_6 nanoparticles have a similar size of 19–22 nm and a specific surface area of 71–77 m^2 g^{-1}. This polyoxoniobate based hydrothermal synthesis method may also be extended to prepare other 3d-TM based tungstate and tantalate columbite nanoparticles. Their catalytic performance for ORR strongly correlates with different types of 3d transition metals incorporated. In particular, $NiNb_2O_6$ demonstrates the best activity for H_2O_2 synthesis with the highest U_{disk} (0.72 V vs RHE) and U_{ring} (0.69 V vs RHE). It retains a selectivity of 96% with the corresponding H_2O_2 Faradaic efficiency of 92% in a wide potential window from 0.2 to 0.6 V versus RHE. The overall catalytic performance of $NiNb_2O_6$ is superior to other transition metal oxide-based catalysts recently reported. Ex situ XPS and operando FTIR spectroscopic studies show that surface Nb atoms in $NiNb_2O_6$ are active catalytic sites. DFT calculations further reveal that the introduction of 3d transition metals shifts the Nb d-band centers, which affects the interaction between Nb and ORR intermediates, resulting in the volcano-shaped

correction between the Nb d-band center and the catalytic activity of MNb_2O_6. The optimal $NiNb_2O_6$ was applied in an H-shaped electrolyzer, which reaches the H_2O_2 productivity of 996 $mmol_{H2O2}$ g_{cat}^{-1} h^{-1}. H_2O_2 containing electrolytes can be directly used to efficiently decompose organic dyes. The 3d transition-metal-mediated columbite nanocatalysts have a low cost and stable, demonstrating excellent application potentials in decentralized H_2O_2 electrosynthesis for many environmental and energy applications. Our work also suggests that the fine-tuning of electronic interaction between transition metal atoms in bimetallic or trimetallic transition metal oxides by doping different 3d transition metals can significantly alter their catalytic activity. This can become a general approach to obtain high-performance electrocatalysts for potential reactions, such as electrochemical H_2O_2 production via 2e$^-$ ORR. Further, the theoretical computation to correlate catalytic performance with the d-band center of transition metals can assist as an efficient tool to guide the selection of different 3d transition metals and their combinations.

4. Experimental Section

Material Synthesis: All chemicals used in this study were obtained from Sigma-Aldrich. Potassium polyoxoniobate ($K_7HNb_6O_{19}·13H_2O$) was synthesized by a molten salt reaction method.[38] Briefly, Nb_2O_5 (99.9, 325 mesh) particles were slowly added into molten KOH at the Nb/K molar ratio of 1/8 in a Ni crucible. After cooling to room temperature, the resulting solid product was dissolved in an ethanol-water solution (v/v = 1) to remove excess KOH, and the unreacted solid residues were removed by filtration. $K_7HNb_6O_{19}$ was precipitated and recrystallized by adding 95% ethanol in the solution, and the resulting crystals were further washed with 95% ethanol before dried in air. Divalent 3d transition metal salts, including $Mn(OAc)_2·4H_2O$, $FeCl_2$, $CoCl_2·6H_2O$, $NiCl_2·4H_2O$, and $Cu(OAc)_2$, were used to synthesize the specific MNb_2O_6 by a hydrothermal method. In a typical synthesis, 0.6 mmol of one type of transition metal salt and 0.2 mmol of $K_7HNb_6O_{19}·13H_2O$ were dissolved separately in 15 mL degassed deionized (DI) water. Next, the transition metal salt solution was added to the $K_7HNb_6O_{19}$ solution dropwise under vigorous stirring and Ar gas bubbling. The mixture was then transferred to a 45 mL Teflon lined hydrothermal reactor (204, Paar), and additional degassed DI water was added to reach a total volume of 36 mL (about 2/3 of the volume of the hydrothermal reactor). After the hydrothermal reaction at 180 °C for 12 h, the resulting solid material was recovered by centrifugation and washing with 95% ethanol and DI water. After drying at 80 °C overnight in a vacuum oven, the solid was annealed at 800 °C in Ar flow (200 sccm) in a tube furnace to obtain columbite nanoparticles.

Two reference catalysts (Nb_2O_5 and NiO) were also prepared for comparison. Nb_2O_5 nanoparticles were synthesized by adding 5 mL of 0.1 M $NbCl_5$ ethanol solution (anhydrous) drop-wisely to 50 mL 0.1 M NH_4OH water solution under vigorous stirring. White precipitates were further aged for 12 h before they were collected and washed by centrifugation. After drying in the vacuum oven at 80 °C overnight, dry powders were annealed in air at 800 °C for 2 h to obtain Nb_2O_5 nanoparticles. NiO was synthesized following a previously reported method.[39] Briefly, $NiCl_2$ was first dissolved in absolute ethanol, and then N_2H_4 was added to the solution at a molar ratio of 5 to Ni^{2+}. The pH of the mixture was adjusted to 12 by adding KOH solution and further stirred for 2 h at room temperature to obtained $Ni(OH)_2·0.5H_2O$ precipitates, which were then collected by filtration and washed with DI water and acetone. After drying under in the vacuum oven at 80 °C overnight, NiO was obtained by the thermal decomposition of dried precipitates at 600 °C in air.

Material Characterization: The elemental composition of different MNb_2O_6 was determined by ICP-AES (Vista Pro, Varian). PXRD patterns were obtained on an XRD diffractometer (Stoe Stadi P) under a Cu Kα source (λ = 1.5406 Å) with a scan step size of 0.01°. STEM and EDX were performed using a microscope (FEI, Themis-Z). XPS spectra were collected using an XPS spectrometer (K-Alpha+, Thermo Fisher Scientific) equipped with an Al-Kα (1486.3 eV) source. All XPS spectra were collected at the pass energy of 20 eV, and the binding energy was corrected with a standard graphite sample. FTIR spectra were measured on an FTIR spectrometer (Nicolet 6700, Thermo Fisher Scientific) in the attenuated total reflection (ATR) mode using a diamond crystal.

Electrochemical Measurements: The different catalyst inks were prepared by dispersing a catalyst at the concentration of 5 mg mL^{-1} in a water/isopropanol (v/v = 1/9) solution containing 0.05% wt% Nafion 117. After bath sonication for 3 h, the catalyst ink was drop-casted on RRDEs with a glassy carbon disk and a Pt ring (Pine Instrument, disk OD = 5.5 mm, ring ID = 6.5 mm, and OD = 8.5 mm) at an aerial mass loading of 200 µg cm^{-2}. All electrochemical measurements were carried out on an electrochemical workstation (760E, CHI) in the three-electrode configuration. A Pt wire (Basi) was used as the counter electrode, an Hg/HgO (0.1 M KOH) electrode as the reference electrode in O_2 saturated 0.1 M KOH (pH = 12.6) electrolyte. The electrolyte temperature was maintained at 25 °C using a water jacket. All reported potentials were corrected against a RHE by adding 0.197 + 0.0591 × pH. LSV polarization curves were collected at a scan rate of 2 mV s^{-1} without iR correction. The disk potential was scanned from 1.1 to 0.1 V versus RHE, while the potential applied on the Pt ring electrode was kept at 1.3 V versus RHE to oxidize produced H_2O_2. The onset potentials for disk and ring electrodes (U_{disk} and U_{ring}) are defined as the potential required to reach a geometric current density of –0.05 mA cm^{-2} for the disk electrode and 0.02 mA cm^{-2} for the ring electrode, respectively.

The selectivity toward H_2O_2 formation ($H_2O_2\%$), ORR electron transfer number (n) and Faradaic efficiency ($FE_{H_2O_2}$, %) were determined by Equations (1–3), as shown below

$$H_2O_2\% = 200 \times \frac{i_{ring}/N}{i_{disk}+i_{ring}/N} \tag{1}$$

$$n = 4 \times \frac{i_{disk}}{i_{disk}+i_{ring}/N} \tag{2}$$

$$FE_{H_2O_2} = \frac{i_{ring}/N}{|i_{disk}|} \times 100 \tag{3}$$

where i_{ring} and i_{disk} are the current obtained from the Pt ring and glassy carbon disk electrodes, respectively. N is the collection efficiency, which was determined as 0.38 after the calibration using the ferrocyanide redox method (see Figure S18 in the Supporting Information). The product-specific current density of H_2O_2 ($j_{H_2O_2}$) and H_2O (j_{H_2O}) was calculated by Equations (4) and (5)

$$j_{H_2O_2} = i_{ring}/(N \times A_{ring}) \tag{4}$$

$$j_{H_2O} = j_{disk} - j_{H_2O_2} \tag{5}$$

A_{ring} is the ring area at 0.236 cm^2.

Tafel analysis was performed by extracting the limiting current density (j_K) from RRDE polarization curves using the Koutecký-Levich (K-L) equation, as shown below (Equation (6))

$$\frac{1}{j} = \frac{1}{j_k} + \frac{1}{0.62nFC_0(D_0)^{2/3}v^{-1/6}\omega^{1/2}} \tag{6}$$

where j is the measured current density, ω is the angular velocity, n is electron transfer number, F is the Faraday constant at 96 485 C mol^{-1}, C_0 is the saturated concentration of O_2 in the electrolyte at room temperature (1.1 × 10^{-6} mol cm^{-3}), D_0 is the diffusion coefficient of O_2

in the electrolytes (1.9 × 10^{-5} cm^2 s^{-1}), and v is the kinematic viscosity of the electrolyte at 25 °C (1 × 10^{-2} cm^2 s^{-1}).

Computational Method: DFT calculations were conducted using the VASP code with spin-polarization and Hubbard-U corrections. The core electrons were described by a projector augmented-wave method.[40] The generalized gradient approximation method was used to describe electron correlation, with the functional developed by Perdew, Burke, and Ernzerhof.[41] Kohn-Sham wave functions expanded in a plane wave basis set were used to describe valence electrons,[42] with a kinetic cut-off of 400 eV. The Brillouin zone was sampled with a (3 × 3 × 1) k-point mesh using the method of Methfessel and Paxton.[43] The use of U_{eff} (U-J) for each system was based on the suggested values from MaterialsProject (https://materialsproject.org/). Convergence was defined as when all the forces of each atom fell below 0.05 eV per Å. Based on the XRD and STEM measurement results, the surfaces of MNb_2O_6 (M = Co, Cu, Fe, Mn, Nb, and Ni) were modelled based on an orthorhombic $FeNb_2O_6$ lattice (acquired from the Materials Project database) by replacing the 3d-metal sites, and slabs exposing (131) facets were adopted for calculation. The d-band centers were calculated as the average of the spin up and down electrons.

H-Shape Electrolyzer and Organic Dye Removal: A gas diffusion layer (GDL, Ø = 3 cm, ≈7 cm^2, Toray Carbon Paper 060) loaded with 500 µg cm^{-2} $NiNb_2O_6$ catalyst was used as the working electrode in the cathode chamber. Pt foil was used as the counter electrode in the anode chamber. An activated Nafion 117 membrane was used to separate the anode and cathode chambers. 0.1 M KOH was used as the electrolyte. The volume of catholyte in the cathode chamber was 30 mL. The concentration of H_2O_2 produced in the cathode chamber was periodically quantified using a titration method by $Ce(SO_4)_2$ solution (Equation (7))

$$2Ce^{4+} + H_2O_2 \rightarrow 2Ce^{3+} + 2H^+ + O_2 \tag{7}$$
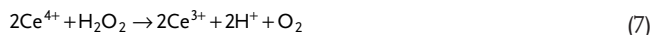
The concentration calibration curve of $Ce^{4+/3+}$ is displayed in Figure S19 in the Supporting Information.

Three organic dyes, methylene blue (MB), rhodamine B (RB), and acid orange 7 (AO7), were dissolved in DI water at the concentration of 20 ppm. After the H-shape electrolyzer was discharging at 35 mA cm^{-2} for 30 min, about 5 mL of the catholyte collected from the cathode chamber was acidified by adding 0.5 mL 1 M H_2SO_4 containing 1 × 10^{-3} M Fe^{2+} and then added into 10 mL of dye solution. The mixture was hand-shaken briefly and kept stationary for 10 min. The dye concentration was determined by measuring their absorption spectra at 685 nm (MB), 553 nm (RB), and 487 nm (AO7), respectively. The absorbance-concentration calibration curves of different dyes are displayed in Figure S20 in the Supporting Information.

Supporting Information

Supporting Information is available from the Wiley Online Library or from the author.

Conflict of Interest

The authors declare no conflict of interest.

Data Availability Statement

The data that support the findings of this study are available on request from the corresponding author. The data are not publicly available due to privacy or ethical restrictions.

Keywords

[1] S. Yang, A. Verdaguer-Casadevall, L. Arnarson, L. Silvioli, V. Čolić, R. Frydendal, J. Rossmeisl, I. Chorkendorff, I. E. L. Stephens, *ACS Catal.* **2018**, *8*, 4064.

[2] R. Ciriminna, L. Albanese, F. Meneguzzo, M. Pagliaro, *ChemSusChem* **2016**, *9*, 3374.

[3] J. C. Kruithof, P. C. Kamp, B. J. Martijn, *Ozone: Sci. Eng.* **2007**, *29*, 273.

[4] V. Russo, R. Tesser, E. Santacesaria, M. Di Serio, *Ind. Eng. Chem. Res.* **2013**, *52*, 1168.

[5] M. L. Bianchi, R. Crisol, U. Schuchardt, *Bioresour. Technol.* **1999**, *68*, 17.

[6] I. A. Balcıoğlu, M. Ötker, *Chemosphere* **2003**, *50*, 85.

[7] C. J. McDonnell-Worth, D. R. MacFarlane, *Aust. J. Chem.* **2018**, *71*, 781.

[8] J. M. Campos-Martin, G. Blanco-Brieva, J. L. Fierro, *Angew. Chem., Int. Ed.* **2006**, *45*, 6962.

[9] a) J. K. Edwards, E. Ntainjua, A. F. Carley, A. A. Herzing, C. J. Kiely, G. J. Hutchings, *Angew. Chem., Int. Ed.* **2009**, *48*, 8512; b) S. J. Freakley, Q. He, J. H. Harrhy, L. Lu, D. A. Crole, D. J. Morgan, E. N. Ntainjua, J. K. Edwards, A. F. Carley, A. Y. Borisevich, *Science* **2016**, *351*, 965.

[10] E. Berl, *Trans. Electrochem. Soc.* **1939**, *76*, 359.

[11] P. C. Foller, R. T. Bombard, *J. Appl. Electrochem.* **1995**, *25*, 613.

[12] a) I. Yamanaka, *J. Jpn. Pet. Inst.* **2014**, *57*, 237; b) Y. Y. Jiang, P. J. Ni, C. X. Chen, Y. Z. Lu, P. Yang, B. Kong, A. Fisher, X. Wang, *Adv. Energy Mater.* **2018**, *8*, 1801909; c) C. Xia, Y. Xia, P. Zhu, L. Fan, H. Wang, *Science* **2019**, *366*, 226.

[13] S. C. Perry, D. Pangotra, L. Vieira, L.-I. Csepei, V. Sieber, L. Wang, C. Ponce de León, F. C. Walsh, *Nat. Rev. Chem.* **2019**, *3*, 442.

[14] a) R. M. Félix-Navarro, M. Beltrán-Gastélum, M. I. Salazar-Gastélum, C. Silva-Carrillo, E. A. Reynoso-Soto, S. Pérez-Sicairos, S. W. Lin, F. Paraguay-Delgado, G. Alonso-Núñez, *J. Nanopart. Res.* **2013**, *15*, 1; b) E. Pizzutilo, O. Kasian, C. H. Choi, S. Cherevko, G. J. Hutchings, K. J. J. Mayrhofer, S. J. Freakley, *Chem. Phys. Lett.* **2017**, *683*, 436; c) S. Siahrostami, A. Verdaguer-Casadevall, M. Karamad, D. Deiana, P. Malacrida, B. Wickman, M. Escudero-Escribano, E. A. Paoli, R. Frydendal, T. W. Hansen, I. Chorkendorff, I. E. Stephens, J. Rossmeisl, *Nat. Mater.* **2013**, *12*, 1137; d) A. Verdaguer-Casadevall, D. Deiana, M. Karamad, S. Siahrostami, P. Malacrida, T. W. Hansen, J. Rossmeisl, I. Chorkendorff, I. E. Stephens, *Nano Lett.* **2014**, *14*, 1603; e) V. S. Antonin, L. S. Parreira, L. R. Aveiro, F. L. Silva, R. B. Valim, P. Hammer, M. R. V. Lanza, M. C. Santos, *Electrochim. Acta* **2017**, *231*, 713; f) J. S. Jirkovsky, I. Panas, E. Ahlberg, M. Halasa, S. Romani, D. J. Schiffrin, *J. Am. Chem. Soc.* **2011**, *133*, 19432.

[15] a) H. W. Kim, M. B. Ross, N. Kornienko, L. Zhang, J. Guo, P. Yang, B. D. McCloskey, *Nat. Catal.* **2018**, *1*, 282; b) Z. Lu, G. Chen, S. Siahrostami, Z. Chen, K. Liu, J. Xie, L. Liao, T. Wu, D. Lin, Y. Liu, T. F. Jaramillo, J. K. Nørskov, Y. Cui, *Nat. Catal.* **2018**, *1*, 156.

[16] a) J. F. Carneiro, R. S. Rocha, P. Hammer, R. Bertazzoli, M. Lanza, *Appl. Catal. A* **2016**, *517*, 161; b) V. S. Pinheiro, E. C. Paz, L. R. Aveiro, L. S. Parreira, F. M. Souza, P. H. C. Camargo, M. C. Santos, *Electrochim. Acta* **2018**, *259*, 865; c) W. R. P. Barros, Q. Wei, G. Zhang, S. Sun, M. R. V. Lanza, A. C. Tavares, *Electrochim. Acta* **2015**, *162*, 263; d) M. H. M. T. Assumpção, R. F. B. De Souza, R. M. Reis, R. S. Rocha, J. R. Steter, P. Hammer, I. Gaubeur, M. L. Calegaro, M. R. V. Lanza, M. C. Santos, *Appl. Catal. B* **2013**, *142-143*, 479; e) M. H. M. T. Assumpção, A. Moraes, R. F. B. De Souza, I. Gaubeur, R. T. S. Oliveira, V. S. Antonin, G. R. P. Malpass, R. S. Rocha, M. L. Calegaro, M. R. V. Lanza, M. C. Santos, *Appl. Catal. A* **2012**, *411-412*, 1; f) A. Moraes, M. H. M. T. Assumpção, R. Papai, I. Gaubeur, R. S. Rocha, R. M. Reis, M. L. Calegaro, M. R. V. Lanza, M. C. Santos, *J. Electroanal. Chem.* **2014**, *719*, 127.

[17] J. F. Carneiro, M. J. Paulo, M. Siaj, A. C. Tavares, M. R. V. Lanza, *J. Catal.* **2015**, *332*, 51.

[18] a) Y. Pang, H. Xie, Y. Sun, M.-M. Titirici, G.-L. Chai, *J. Mater. Chem. A* **2020**, *8*, 24996; b) K. Dong, Y. Wei, H. T. Zhao, J. Liang, P. Ding, Q. Liu, Z. Q. Xu, S. Y. Lu, Q. Li, X. P. Sun, *J. Mater. Chem. A* **2020**, *8*, 23123.

[19] a) Z.-J. Zhao, S. Liu, S. Zha, D. Cheng, F. Studt, G. Henkelman, J. Gong, *Nat. Rev. Mater.* **2019**, *4*, 792; b) Y. Jiao, Y. Zheng, M. Jaroniec, S. Z. Qiao, *Chem. Soc. Rev.* **2015**, *44*, 2060; c) Y. Zhou, Z. Zhou, R. Shen, R. Ma, Q. Liu, G. Cao, J. Wang, *Energy Storage Mater.* **2018**, *13*, 189; d) R. B. Rankin, J. Greeley, *ACS Catal.* **2012**, *2*, 2664.

[20] M. B. Zakaria, C. Li, M. Pramanik, Y. Tsujimoto, M. Hu, V. Malgras, S. Tominaka, Y. Yamauchi, *J. Mater. Chem. A* **2016**, *4*, 9266.

[21] M. B. Pinto, A. L. Soares, M. C. Quintão, H. A. Duarte, H. A. De Abreu, *J. Phys. Chem. C* **2018**, *122*, 6618.

[22] A. V. Besserguenev, M. H. Dickman, M. T. Pope, *Inorg. Chem.* **2001**, *40*, 2582.

[23] S. Lei, C. Wang, D. Guo, X. Gao, D. Cheng, J. Zhou, B. Cheng, Y. Xiao, *RSC Adv.* **2014**, *4*, 52740.

[24] M. C. Biesinger, B. P. Payne, A. P. Grosvenor, L. W. M. Lau, A. R. Gerson, R. S. C. Smart, *Appl. Surf. Sci.* **2011**, *257*, 2717.

[25] a) T. Yamashita, P. Hayes, *Appl. Surf. Sci.* **2008**, *254*, 2441; b) J. Liu, Y. Ji, J. Nai, X. Niu, Y. Luo, L. Guo, S. Yang, *Energy Environ. Sci.* **2018**, *11*, 1736.

[26] M. C. Biesinger, B. P. Payne, L. W. M. Lau, A. Gerson, R. S. C. Smart, *Surf. Interface Anal.* **2009**, *41*, 324.

[27] M. C. Biesinger, *Surf. Interface Anal.* **2017**, *49*, 1325.

[28] a) J. Gao, H. b. Yang, X. Huang, S.-F. Hung, W. Cai, C. Jia, S. Miao, H. M. Chen, X. Yang, Y. Huang, T. Zhang, B. Liu, *Chem* **2020**, *6*, 658; b) B. Sarkar, B. K. Barman, K. K. Nanda, *ACS Appl. Energy Mater.* **2018**, *1*, 1116.

[29] a) J. K. Nørskov, J. Rossmeisl, A. Logadottir, L. Lindqvist, J. R. Kitchin, T. Bligaard, H. Jónsson, *J. Phys. Chem. B* **2004**, *108*, 17886; b) M. T. M. Koper, *J. Solid State Electrochem.* **2013**, *17*, 339.

[30] J.-C. Dupin, D. Gonbeau, P. Vinatier, A. Levasseur, *Phys. Chem. Chem. Phys.* **2000**, *2*, 1319.

[31] G. Mattioli, F. Filippone, A. Amore Bonapasta, *J. Am. Chem. Soc.* **2006**, *128*, 13772.

[32] R. Nakamura, A. Imanishi, Y. Murakoshi, Y. Nakato, *J. Am. Chem. Soc.* **2003**, *125*, 7443.

[33] a) V. R. Stamenkovic, B. S. Mun, M. Arenz, K. J. Mayrhofer, C. A. Lucas, G. Wang, P. N. Ross, N. M. Markovic, *Nat. Mater.* **2007**, *6*, 241; b) V. Stamenkovic, B. S. Mun, K. J. Mayrhofer, P. N. Ross, N. M. Markovic, J. Rossmeisl, J. Greeley, J. K. Nørskov, *Angew. Chem.* **2006**, *118*, 2963.

[34] a) H. Lee, O. Gwon, K. Choi, L. Zhang, J. Zhou, J. Park, J.-W. Yoo, J.-Q. Wang, J. H. Lee, G. Kim, *ACS Catal.* **2020**, *10*, 4664; b) J.-H. Lee, D. Yim, J. H. Park, C. H. Lee, J.-M. Ju, S. U. Lee, J.-H. Kim, *J. Mater. Chem. A* **2020**, *8*, 13490; c) Z. Xu, J. R. Kitchin, *J. Chem. Phys.* **2015**, *142*, 104703; d) Z. Xu, J. R. Kitchin, *Catal. Commun.* **2014**, *52*, 60; e) M. García-Mota, A. Vojvodic, F. Abild-Pedersen, J. K. Nørskov, *J. Phys. Chem. C* **2013**, *117*, 460.

[35] A. J. Medford, A. Vojvodic, J. S. Hummelshøj, J. Voss, F. Abild-Pedersen, F. Studt, T. Bligaard, A. Nilsson, J. K. Nørskov, *J. Catal.* **2015**, *328*, 36.

[36] B. Hammer, J. K. Norskov, *Nature* **1995**, *376*, 238.

[37] H. T. Chung, D. A. Cullen, D. Higgins, B. T. Sneed, E. F. Holby, K. L. More, P. Zelenay, *Science* **2017**, *357*, 479.

[38] C. M. Flynn, G. D. Stucky, *Inorg. Chem.* **1969**, *8*, 332.

[39] M. El-Kemary, N. Nagy, I. El-Mehasseb, *Mater. Sci. Semicond. Process.* **2013**, *16*, 1747.

[40] P. E. Blöchl, *Phys. Rev. B* **1994**, *50*, 17953.

[41] J. P. Perdew, K. Burke, M. Ernzerhof, *Phys. Rev. Lett.* **1996**, *77*, 3865.

[42] W. Kohn, L. J. Sham, *Phys. Rev.* **1965**, *140*, A1133.

[43] H. J. Monkhorst, J. D. Pack, *Phys. Rev. B* **1976**, *13*, 5188.